

Enhanced Zinc Ion Storage Capability of V₂O₅ Electrode Materials with Hollow Interior Cavities

Yi Liu,^[a] Ying Liu,^[a] Yusuke Yamauchi,^[b, c, d] Zeid A. Alothman,^[e] Yusuf Valentino Kaneti,*^[c] and Xiang Wu*^[a]

This work was supported by National Natural Science Foundation of China (No. 52172218) and the JST-ERATO Materials Space-Tectonics Project (JPMJER2003). Z.A. is grateful to the Researchers Supporting Project (RSP-2021/1), King Saud University, Riyadh, Saudi Arabia. This work was performed in part at

the Queensland node of the Australian National Fabrication Facility, a company established under the National Collaborative Research Infrastructure Strategy to provide nano and micro-fabrication facilities for Australia's researchers.

1. Introduction

With the aggravation of energy crisis, the development of renewable energy sources is becoming increasingly important.^[1] However, some energy sources, such as wind, solar and tidal power, are intermittent in nature, leading to their inability to meet the demand of distributed smart grid.^[2–4] Lithium-ion batteries (LIBs) have been widely used in electrical energy storage owing to their remarkable energy density and excellent cyclability.^[5] However, the limited lithium supply, high cost, and low safety of LIBs have restricted their applications in large-scale energy storage systems.^[6] Therefore, it is especially important to develop alternatives to LIBs.^[7,8] In recent years, a variety of rechargeable aqueous metal-ion batteries (Na, K, Zn, Ca and Al)^[9,10] have been reported. Among them, aqueous zinc-ion batteries (AZIBs) showed some promise because of the wide abundance of zinc source and the use of mild aqueous electrolytes.^[11–13]

To date, a series of cathode materials have been developed for AZIBs, such as manganese-based oxides,^[14,15] Prussian blue

analogues^[16,17] and vanadium-based materials.^[18,19] Unfortunately, manganese-based materials suffer from poor cycling stability and rate performance.^[20] Prussian blue analogues (PBAs) with open frame structures can provide enough space for Zn²⁺ insertion, but the low capacity impedes their practical applications.^[21] The multiple valence states of vanadium (V) elements endow V-based materials with different crystal structures.^[22,23] Thus, V-based compounds typically show high capacities and superior cycling life. For example, Kim and co-workers synthesized Zn₂V₂O₇ nanowires with 85% capacity retention after 1,000 cycles at 4 A g⁻¹.^[24] He et al. prepared V₂O₅ nanosheets supported on three-dimensional (3D) N-doped carbon nanowall arrays as a potential cathode material for AZIBs, which showed a capacity retention of 85.3% after 400 cycles at 6 A cm⁻³.^[25] V₂O₅ nanobelts exhibited a moderate capacity of 370 mAh g⁻¹ at 0.2 A g⁻¹.^[26] Despite some progress, the capacities of these V₂O₅ materials are still far from the theoretical capacity of V₂O₅ (589 mAh g⁻¹).

Herein, we prepare V₂O₅ hollow spheres for zinc-ion storage by a simple solvothermal strategy. The unique hollow structure of these V₂O₅ spheres can provide abundant reaction sites and shorten the diffusion paths of electrons and ions. The as-obtained V₂O₅ hollow spheres deliver a high specific capacity of 437.5 mAh g⁻¹ at a current density of 0.2 A g⁻¹ and a reversible rate capacity of 92.6%. Moreover, they can maintain 85.3% of the initial capacity after 1,500 cycles at 5 A g⁻¹. The assembled cell exhibits an energy density (of 306.25 Wh kg⁻¹) at a power density of 140 W kg⁻¹. The high specific capacity and excellent cyclability of the fabricated Zn/V₂O₅ battery can be ascribed to the excellent Zn²⁺ insertion/extraction ability of these V₂O₅ hollow spheres.

2. Result and Discussion

2.1. Structural and Composite Characterization

The as-obtained V₂O₅ was annealed in air at 350 °C and 450 °C with a heating rate of 0.5 °C min⁻¹ for 2 h. The resulting

[a] Y. Liu, Y. Liu, Prof. X. Wu
School of Materials Science and Engineering
Shenyang University of Technology
Shenyang 110870, China
E-mail: wuxiang05@sut.edu.cn

[b] Y. Yamauchi
School of Chemical Engineering
University of Queensland
Brisbane, QLD, 4072, Australia

[c] Y. Yamauchi, Y. V. Kaneti
Australian Institute for Bioengineering and Nanotechnology (AIBN)
University of Queensland
Brisbane, QLD, 4072, Australia
E-mail: v.kaneti@uq.edu.au

[d] Y. Yamauchi
JST-ERATO Yamauchi Materials Space-Tectonics Project and International Center for Materials Nanoarchitectonics (WPI-MANA)
National Institute for Materials Science (NIMS)
1-1 Tsukuba, Ibaraki 305-0044, Japan

[e] Z. A. Alothman
Department of Chemistry, College of Science
King Saud University
Riyadh 11451, Saudi Arabia

products are named as V_2O_5 -350 and V_2O_5 -450, respectively. The phase composition and purity of the as-prepared samples were investigated by X-ray diffraction (XRD). Figure 1(a) shows the presence of strong diffraction peaks which are consistent with orthorhombic V_2O_5 with a $Pmmn$ (59) space group (PDF card No. 41-1426). This indicates the high purity and good crystallinity of the as-prepared V_2O_5 samples. The lattice parameters are $a=11.51\text{ \AA}$, $b=3.56\text{ \AA}$ and $c=4.37\text{ \AA}$. As shown in the inset of Figure 1(a), the crystal structure consists of many VO_5 tetragonal pyramids by sharing edges and corners. The large interlayer spacing of V_2O_5 can provide a convenient transport path for Zn^{2+} .

X-ray photoelectron spectroscopy (XPS) was used to characterize the surface valence states of the products. The XPS survey spectra in Figure 1(b) confirm the presence of V and O in V_2O_5 -350. From Figure 1(c), it can be observed that the V $2p_{3/2}$ and V $2p_{1/2}$ peaks are located at 516.7 and 523.8 eV, respectively, which correspond to V^{5+} .^[27] In addition, V^{4+} peaks are also observed at 516.1 and 524.3 eV.^[28] According to a previous report,^[29] V_2O_5 with mixed vanadium valences (V^{4+} and V^{5+}) showed high electrochemical activity, low polarization,

and fast ion diffusion. The O 1s spectrum shows peaks at 529.5 and 530.5 eV which can be assigned to V–O and hydroxyl (OH^-) group, respectively (Figure 1d).^[30]

The specific surface areas of V_2O_5 -350 and V_2O_5 -450 samples are measured to be 12.89 and $12.53\text{ m}^2\text{ g}^{-1}$, respectively, as determined by nitrogen adsorption-desorption measurements (Figure 1e and f). The total pore volume ($0.057\text{ cm}^3\text{ g}^{-1}$) of V_2O_5 -350 is larger than that of V_2O_5 -450 ($0.047\text{ cm}^3\text{ g}^{-1}$). Clear capillary condensation is not observed on the adsorption isotherm, indicating the presence of mixed porosity.

The morphology of the as-prepared V_2O_5 samples were investigated by scanning electron microscopy (SEM) and transmission electron microscopy (TEM). V_2O_5 -350 shows spherical structure with an average diameter of 350 nm, as shown in Figure 2(a and b). In comparison, V_2O_5 -450 exhibits uneven spherical morphology [Figure 2(c and d)], and the surface of these spheres is changed from a flaky shape to an irregular block-like shape. These observations suggest the possible collapse of the V_2O_5 structural framework with increasing annealing temperature. Furthermore, the TEM analysis reveals that the prepared V_2O_5 -350 spheres exhibit hollow interiors and

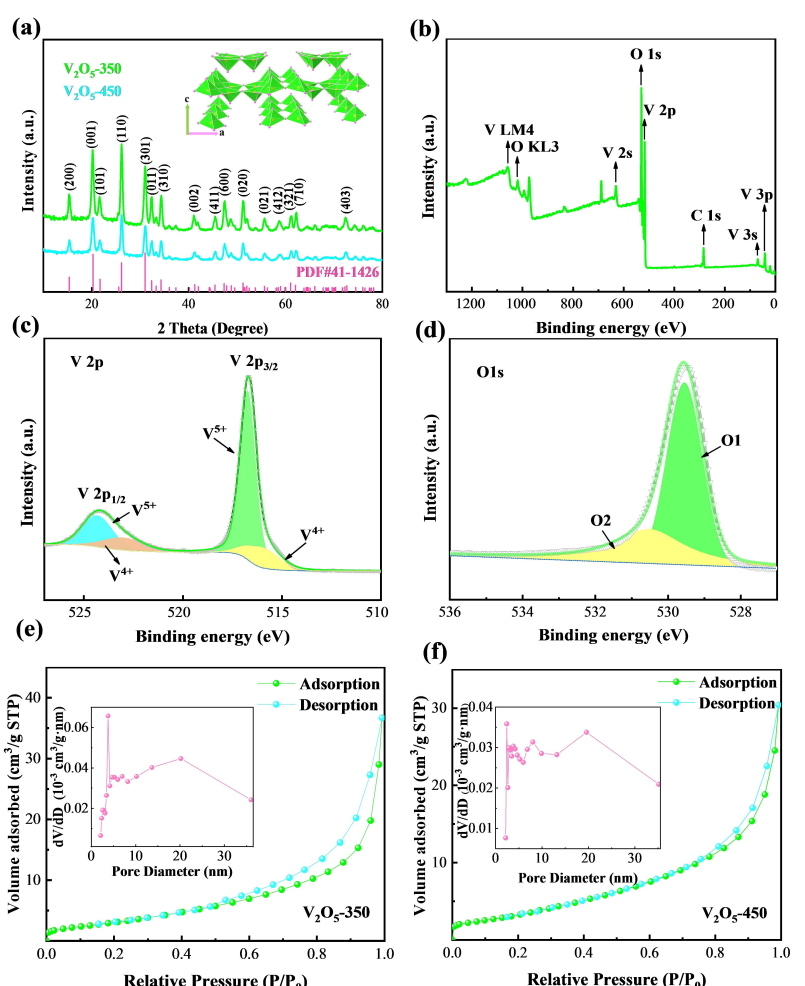


Figure 1. Structural and compositional characterizations of as-prepared V_2O_5 samples. a) XRD patterns, b) XPS survey spectra of V_2O_5 -350, and high-resolution c) Volume adsorbed ($\text{cm}^3/\text{g STP}$) d) O 1s spectra of V_2O_5 -350. N_2 adsorption-desorption isotherms and the corresponding pore size distribution (insets) of e) V_2O_5 -350 and f) V_2O_5 -450.

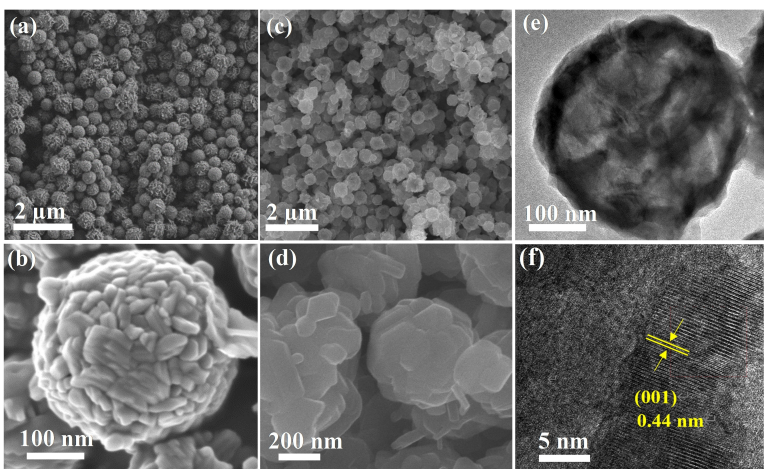


Figure 2. Morphological characterizations of as-prepared V_2O_5 products. SEM images of a,b) V_2O_5 -350 and c,d) V_2O_5 -450 and e,f) TEM images of V_2O_5 -350.

possess large internal space [Figure 2(e)]. The hollow architecture of these spheres can effectively relieve the structural stress caused by ion insertion/extraction or surface Faradaic reaction during repeated charge and discharge processes.^[31] The interplanar spacing of 0.44 nm matches well with the (001) plane of orthorhombic V_2O_5 , confirming its good crystallinity [Figure 2(f)].

2.2. Electrochemical Performance

The electrochemical performance of the V_2O_5 -350 electrode was investigated by CV measurements in the voltage range of 0.2 to 1.6 V with a scan rate of 0.5 mV s^{-1} . CV curves of the V_2O_5 -350 electrode [Figure 3(a)] show two pairs of redox peaks at 0.51/0.88 V and 0.86/1.07 V in the initial three cycles which

correspond to multi-step intercalation/de-intercalation of Zn^{2+} . In addition, the overlapping of the CV curves indicates the high reversibility of the redox reaction. The cycling performances of $\text{Zn}/\text{V}_2\text{O}_5$ -350 and $\text{Zn}/\text{V}_2\text{O}_5$ -450 at current density of 0.2 A g^{-1} are shown in Figure 3(b). The initial discharge capacity of the V_2O_5 -350 electrode is 407 mAh g^{-1} . After 7 cycles, its specific capacity increases to 437.5 mAh g^{-1} . A similar “activation process” has also been observed in a previous report,^[32] which may be related to the unique hollow structures. In subsequent cycles, the capacity is significantly reduced, likely due to some zinc ions located at Zn^{2+} “dead” sites which cannot be extracted from V_2O_5 lattice during the charging process.^[33] In comparison to V_2O_5 -350, the V_2O_5 -450 electrode shows a lower specific capacity of 221.8 mAh g^{-1} at 0.2 A g^{-1} .

GCD curves of the V_2O_5 -350 electrode are given in Figure 3(c). The specific capacity of this electrode reaches its

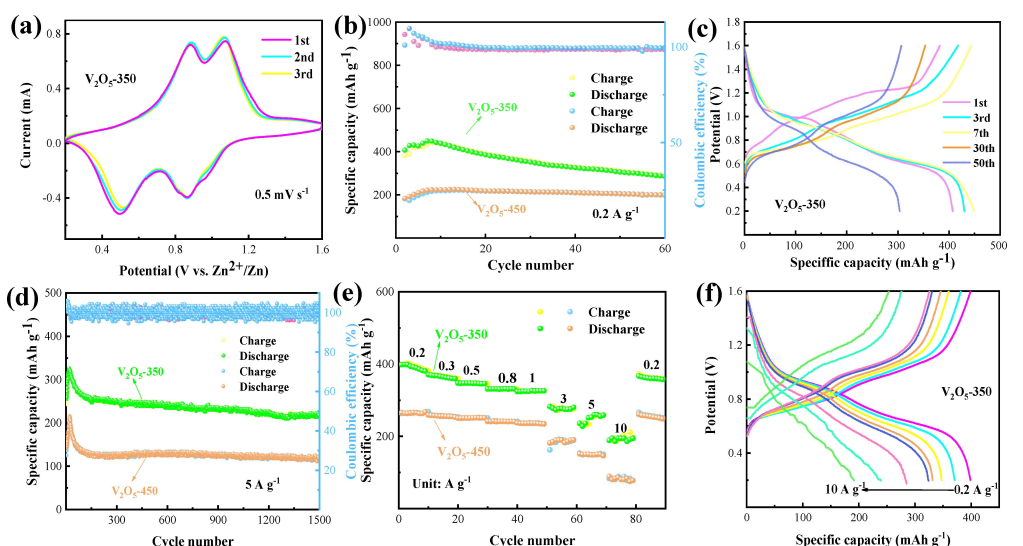


Figure 3. Electrochemical performance of V_2O_5 -350 for AZIB. a) CV curves of V_2O_5 -350 electrode at 0.5 mVs^{-1} . b) Cycling performance and c) GCD curves of V_2O_5 -350 and V_2O_5 -450 electrodes at 0.2 A g^{-1} . d) Cycling performance of V_2O_5 -350 and V_2O_5 -450 electrodes at 5 A g^{-1} . e) Rate capabilities of V_2O_5 -350 and V_2O_5 -450 electrodes at different current densities. f) Specific capacities of V_2O_5 -350 electrode at various current densities.

maximum value at the 7th cycle, which remains at 309.5 mAh g^{-1} after 50 cycles. The energy density of the active electrode material is determined from the GCD curves, and it can be calculated via Equations (1) and (2):

$$E (\text{Wh kg}^{-1}) = QU/2m \quad (1)$$

$$P (\text{W kg}^{-1}) = iU/2m \quad (2)$$

where Q denotes discharge capacity (Ah), m is the mass of active material (kg), i and U are the discharge current (A) and the main operating voltage (V), respectively. The V_2O_5 -350 electrode exhibits a high energy density of $306.25 \text{ Wh kg}^{-1}$ at a power density of 140 W kg^{-1} . It retains 85.3% of the initial discharge capacity after 1,500 cycles at 5 A g^{-1} [Figure 3(d)]. In comparison, the V_2O_5 -450 electrode shows a lower capacity retention of 81.3% after 1,500 cycles at 5 A g^{-1} .

The rate performance of an electrode material is also important for evaluating the total properties of batteries. From Figure 3(e), the reversible capacities of the V_2O_5 -350 electrode are 398.6 , 370.4 , 347.3 , 330.8 , 324.5 , 277.3 , 252.7 , and 197.2 mAh g^{-1} at 0.2 , 0.3 , 0.5 , 0.8 , 1 , 3 , 5 , and 10 A g^{-1} , respectively. When the current density is returned to 0.2 A g^{-1} , the capacity recovers to 377.3 mAh g^{-1} , corresponding to capacity retention of 92.6%. This implies that the V_2O_5 -350 electrode possesses a highly reversible rate capability. In comparison, the reversible capacities of the V_2O_5 -450 electrode are 264 , 255.8 , 251 , 241.1 , 236.4 , 189.7 , 150.2 and 86.1 mAh g^{-1} at 0.2 , 0.3 , 0.5 , 0.8 , 1 , 3 , 5 , and 10 A g^{-1} , respectively, which are lower than those of V_2O_5 -350 electrode.

Figure 3(f) shows the corresponding charge-discharge curves at different current densities. Two charge-discharge plateaus are observed at around $1.0/0.9$ and $0.7/0.6 \text{ V}$, corresponding to electronic redox and the extraction/insertion of Zn^{2+} in host materials, respectively. The flake-like surface of V_2O_5 -350 may provide additional active sites to improve the overall electrochemical performance of the AZIB. The zinc-ion storage performance of the prepared V_2O_5 -350 electrode is superior to many previously reported vanadium-based materials, as shown in Table 1.^[34–42]

2.3. Energy Storage Kinetics

To understand the zinc-ion storage behavior of the V_2O_5 -350 electrode, the electrochemical reaction kinetics was investigated in detail. Figure 4(a) shows CV curves of the V_2O_5 -350 electrode at scan rates of 0.2 , 0.4 , 0.6 , 0.8 , and 1 mVs^{-1} . It can be observed that the shape of the CV curves remains almost similar with increasing scan rate. With increasing scan rate, the oxidation and reduction peaks move towards high and low potentials, respectively. Based on the CV curves at different scan rates, the electrochemical kinetics process can be analyzed by Equation (3):^[43]

$$i = av^b \quad (3)$$

where i and v represent current and scan rate, respectively, while a and b are adjustable parameters. When $b=0.5$, the reaction process is a diffusion-controlled one. If the b value is in the range of 0.5 to 1 , the electrode material shows both battery and pseudocapacitive properties; when $b \geq 1$, the electrode material possesses a full capacitive behavior.^[44] The b values of the four redox peaks are 0.93 , 0.70 , 0.86 , and 0.73 (Figure 4b). This finding reveals that the electrochemical reaction of $\text{Zn}/\text{V}_2\text{O}_5$ -350 batteries is mostly dominated by surface-controlled capacitance. In addition, Equation (3) can also be expressed by Equation (4):

$$i(V) = k_1v + k_2v^{1/2} \quad (4)$$

where k_1v and $k_2v^{1/2}$ represent capacitive-controlled and diffusion-controlled reactions, respectively.^[45] According to Equation (4), the contribution ratios of the two electrode materials at 1.0 mVs^{-1} are 93.1% and 92% of the total capacity, respectively, indicating their fast redox reactions [Figure 4(c)].

EIS results of the as-prepared V_2O_5 electrodes are given in Figure 4(d). The Nyquist plot of an electrode typically consists of a semicircle in high-frequency region and a slope line in low-frequency region. The semicircle represents charge transfer resistance (R_{ct}) at the electrolyte interface, while the slope line is Warburg impedance (Z_w) corresponding to Zn^{2+} diffusion in cathode material. The R_{ct} of the V_2O_5 -350 electrode (671Ω) is smaller than that of V_2O_5 -450 electrode (798Ω), indicating its superior conductivity. In the low-frequency region, the former shows a higher slope than the latter. This implies that the

Table 1. Comparison of vanadium-base materials for zinc-ion batteries.

Materials	Morphology	Current density [A g^{-1}]	Discharge capacity [mAh g^{-1}]	Electrolyte [M] ZnSO_4	Ref.
V_2O_5	Hollow spheres	0.2	280	3.65	[34]
V_2O_5	Hollow spheres	0.1	327	3	[35]
$\text{Ni}_{0.25}\text{V}_2\text{O}_5 \cdot \text{nH}_2\text{O}$	Nanometers	0.2	389	3	[36]
$\text{VO}_2(\text{B})$	Nanorods	0.1	359	1	[37]
$\text{Zn}_{0.25}\text{V}_2\text{O}_5 \cdot \text{nH}_2\text{O}$	Nanobelts	0.3	282	1	[38]
$\text{K}_2\text{V}_6\text{O}_{16} \cdot 2.7\text{H}_2\text{O}$	Nanorods	0.2	217	1	[39]
VSe_2	Nanosheets	0.1	132	2	[40]
LiV_3O_8	Flake-like particles	0.015	267	1	[41]
$\text{V}_2\text{O}_{5x}/\text{PANI}$	Nanosheets	0.1	400	2	[42]
V_2O_5	Hollow spheres	0.2	437	3	This work

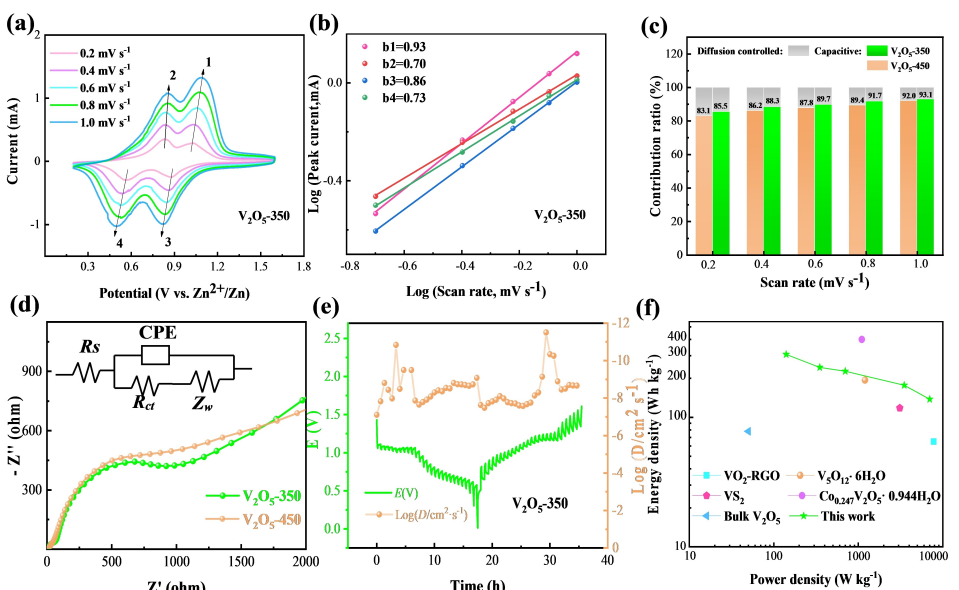


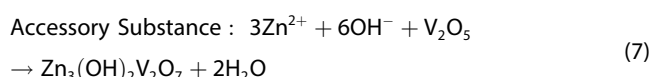
Figure 4. Energy storage kinetics of V₂O₅ electrodes for AZIB. a) CV curves and b) log(*i*) versus log(*v*) of V₂O₅-350 electrode. c) The capacitive contribution ratios of V₂O₅-350 and V₂O₅-450 electrodes at various scan rates. d) Nyquist plots of V₂O₅-350 and V₂O₅-450 electrodes. e) GITT curves and the corresponding Zn²⁺ diffusion coefficient of V₂O₅-350 electrode versus Zn²⁺/Zn in the first charge/discharge process. f) Ragone plot of V₂O₅-350 electrode compared to previously reported electrodes for AZIBs.

transfer of Zn²⁺ ions is faster in the V₂O₅-350 electrode. During the intercalation/de-intercalation of Zn²⁺, the D_{Zn} value is calculated to be 10⁻⁷–10⁻¹² cm²s⁻¹ (Figure 4e), suggesting that Zn²⁺ ions are well-inserted in the host V₂O₅ material. The Ragone plots of several recently reported materials (VO₂-RGO,^[46] V₅O₁₂·6H₂O,^[47] VS₂,^[48] Co_{0.247}V₂O₅·0.944H₂O^[49] and bulk V₂O₅^[50] are shown in Figure 4(f). The assembled Zn/V₂O₅-350 battery shows both high power density and energy density.

2.4. Post-Analysis after Charge/Discharge Process

The post-compositional and structural analyses of the V₂O₅-350 electrode after the charge/discharge process are shown in Figure 5. Figure 5(a) shows the structural transformation of the V₂O₅-350 electrode based on an ex-situ XRD measurement during the 2nd cycle. The (001), (110), (301), and (310) crystal planes originate from the diffraction peaks of the original V₂O₅-350 sample. A series of highly reversible changes is observed after charge/discharge process. In particular, the (110) characteristic peak at 26.18° is shifted to a higher angle during discharging. This suggests that the lattice spacing of the sample becomes larger. This lattice expansion may be attributed to the strong electrostatic interaction between the inserted Zn²⁺ and vanadium-oxygen layer. In the fully charged state, the characteristic peak returns to the initial state, suggesting its reversible structural evolution process. Moreover, the V₂O₅-350 cathode undergoes an activation process during the 2nd cycle. Owing to the dissociation of water, Zn₃V₂O₇(OH)₂·2H₂O is generated as an intermediate product. To

better understand the charge-discharge process, the electrode reactions can be expressed as:



XPS was again used to investigate the changes in elemental states of the V₂O₅-350 electrode during cycling. As seen in Figure 5(b), the presence of Zn 2p_{3/2}/2p_{1/2} spin-orbit doublets in the discharge state confirms the successful intercalation of Zn²⁺ into the V₂O₅ host. During charging state, the intensity of the Zn 2p signal peak is far below that of the discharging state, suggesting the extraction of Zn²⁺ from the host material. As seen in Figure 5(c), both the charge and discharge states of the V₂O₅-350 electrode show the co-existence of V⁴⁺ and V⁵⁺ species. In the charging state, the intensities of V⁵⁺ peaks increase, while those of V⁴⁺ decrease. It can be deduced that most of V⁴⁺ species is oxidized to V⁵⁺ with the de-intercalation of Zn²⁺. The structural characteristics of the V₂O₅-350 electrode after the charge/discharge process were further evaluated by TEM. TEM images of the V₂O₅-350 electrode discharged to 0.2 V and charged to 1.6 V reveal that the V₂O₅-350 electrode still maintains its hollow structure [Figure 5(d and f)]. The interplanar spacing of (001) is 0.46 nm at the discharged state and decreases to 0.42 nm at the charged state of 1.6 V [Figure 5(e and 5g)]. This confirms the successful migration of Zn²⁺ in the V₂O₅-350 cathode.

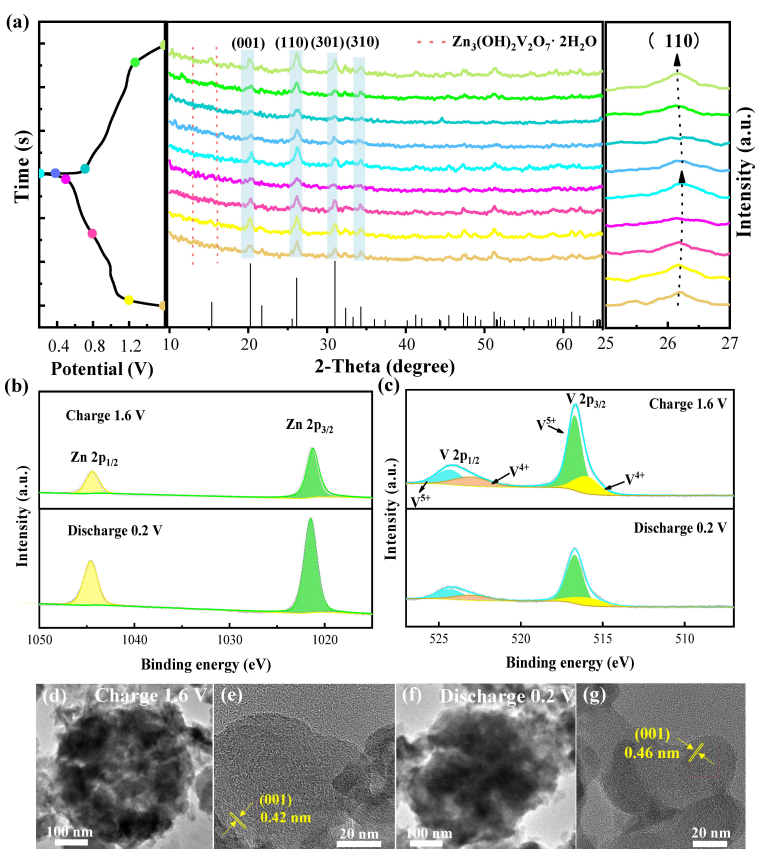


Figure 5. Post-analysis of V_2O_5 -350 electrode after charge/discharge process. a) Ex-situ XRD patterns of V_2O_5 -350 electrode at various charge/discharge states. b,c) XPS spectra of V_2O_5 -350 electrode after charging at 1.6 V and discharging at 0.2 V. TEM images of V_2O_5 -350 electrode d,e) after charging at 1.6 V and f,g) discharging at 0.2 V.

3. Conclusions

In summary, we have synthesized two kinds of V_2O_5 hollow spheres by optimizing the calcination temperature. The as-obtained V_2O_5 -350 electrode exhibits both high specific capacity (437.5 mAh g^{-1} at 0.2 A g^{-1}) and high energy density (306.25 Wh kg^{-1} at a power density of 140 W kg^{-1}). The outstanding electrochemical performance of the V_2O_5 -350 electrode in AZIBs can be attributed to its hollow interior, which can buffer the lattice expansion of the V_2O_5 electrode and accommodate the structural change, while also promoting fast electronic/ionic transport. In addition, the electrochemical kinetics results show that the chemical diffusion of Zn^{2+} in the V_2O_5 -350 electrode is superior to that in V_2O_5 -450 electrode.

Experimental Section

Electrode preparation

In a typical procedure, 1.5 mmol of ammonium metavanadate (NH_4VO_3) was dissolved in 40 mL of absolute ethanol and continuously stirred for 1 h. Next, 1 mL of concentrated nitric acid (68 wt.%) was added dropwise and the resulting mixture solution was vigorously stirred for another 1 h. After that, the mixture solution was transferred into a 100 mL Teflon-lined autoclave and

kept at 180 °C for 24 h. After naturally cooled to room temperature, the as-synthesized product was collected and rinsed with deionized water and ethanol and dried at 60 °C for 24 h. Finally, the as-obtained precursor was annealed in air at 350 °C and 450 °C with a heating rate of 0.5 °C min $^{-1}$ for 2 h. The resulting products are named as V_2O_5 -350 and V_2O_5 -450, respectively.

Structural characterization

X-ray powder diffraction (XRD) patterns were recorded on a powder X-ray diffractometer (Shimadzu-7000, Cu K_α radiation, $\lambda = 0.1541 \text{ nm}$). The specific surface area and the pore size distribution of the samples were measured by nitrogen adsorption-desorption measurements (JW-BK 200 C). The morphologies and microstructures of the products were observed by scanning electron microscope (SEM, Gemini 300-71-31) and transmission electron microscope (TEM, JEM-2100 PLUS). X-ray photoelectron spectroscopy (XPS) (ESCALAB250Xi, Thermo Scientific) was used to analyze the surface elemental states of the samples.

Electrochemical measurements

The cathodes were prepared by mixing the prepared samples (V_2O_5 -350 and V_2O_5 -450), carbon black (super P) and polytetrafluoroethylene (PTFE) with a mass ratio of 7:2:1. Then, these cathodes were dried in a vacuum oven at 60 °C for 12 h and pressed onto a carbon paper. The anode was a zinc flake with a thickness of 0.2 mm. 3 M ZnSO_4 solution was used as the electrolyte. Next, some 2032-type coin cells were assembled at room

temperature. The electrochemical performance was evaluated in a voltage window varying from 0.2 to 1.6 V. The galvanostatic charge-discharge (GCD) curves, galvanostatic intermittent titration technique (GITT), and cyclability were subsequently characterized with a LAND-2100 automatic battery tester. Finally, cyclic voltammetry (CV) and electrochemical impedance spectroscopy (EIS) data were obtained using an electrochemical workstation (CHI-660E). The average mass of the cathode was 1.1 mg. All electrochemical measurements were performed at room temperature (25 °C).

Conflict of Interest

The authors declare no conflict of interest.

Keywords: Vanadium oxide • Zinc-ion batteries • Cathode material • Hollow spheres • High performance electrodes

- [1] T. Liu, X. Cheng, H. Yu, H. Zhu, N. Peng, R. Zheng, J. Zhang, M. Shui, Y. Cui, J. Shu, *Energy Storage Mater.* **2019**, *18*, 68–91.
- [2] D. Zhao, M. Dai, Y. Zhao, H. Liu, Y. Liu, X. Wu, *Nano Energy* **2020**, *72*, 104715.
- [3] H. Li, L. Ma, C. Han, Z. Wang, Z. Liu, Z. Tang, C. Zhi, *Nano Energy* **2019**, *62*, 550–587.
- [4] X. Wu, S. Yao, *Nano Energy* **2017**, *42*, 143–150.
- [5] C. N. Im, C. H. Choi, H. R. Yu, T. Y. Ahn, H. K. Yoon, J. S. Yeo, J. H. Cho, *Batteries Supercaps* **2021**, *4*, 304–315.
- [6] J. Yao, Y. Li, R. C. Massé, E. Uchaker, G. Cao, *Energy Storage Mater.* **2018**, *11*, 205–259.
- [7] Y. Liu, P. Hu, H. Liu, X. Wu, C. Zhi, *Mater. Today* **2020**, *17*, 100431.
- [8] C. Heubner, K. Nikolowski, S. Reuber, M. Schneider, M. Wolter, A. Michaelis, *Batteries Supercaps* **2021**, *4*, 268–285.
- [9] Y. Liu, X. Wu, *J. Energy Chem.* **2021**, *56*, 223–237.
- [10] H. Wang, R. Tan, Z. Yang, Y. Feng, X. Duan, J. Ma, *Adv. Energy Mater.* **2020**, *11*, 2000962.
- [11] C. Zhu, G. Fang, J. Zhou, J. Guo, Z. Wang, C. Wang, J. Li, Y. Tang, S. Liang, *J. Mater. Chem. A* **2018**, *6*, 9677–9683.
- [12] F. Wan, Z. Niu, *Angew. Chem. Int. Ed.* **2019**, *58*, 16358–16367; *Angew. Chem.* **2019**, *131*, 16508–16517.
- [13] C. Deng, X. Xie, J. Han, Y. Tang, J. Gao, C. Liu, X. Shi, J. Zhou, S. Liang, *Adv. Funct. Mater.* **2020**, *30*, 2000599.
- [14] N. Zhang, F. Cheng, Y. Liu, Q. Zhao, K. Lei, C. Chen, X. Liu, J. Chen, *J. Am. Chem. Soc.* **2016**, *138*, 12894–12901.
- [15] C. Xu, B. Li, H. Du, F. Kang, *Angew. Chem. Int. Ed.* **2012**, *51*, 933–935; *Angew. Chem.* **2012**, *124*, 957–959.
- [16] L. Zhang, L. Chen, X. Zhou, Z. Liu, *Adv. Energy Mater.* **2015**, *5*, 1400930.
- [17] L. J. Gao, X. L. Liu, J. Q. Zhang, S. Q. Wang, J. F. Chen, *Mater. Chem. Phys.* **2004**, *88*, 27–31.
- [18] X. Wang, Y. Li, S. Wang, F. Zhou, P. Das, C. Sun, S. Zheng, Z. S. Wu, *Adv. Energy Mater.* **2020**, *10*, 2000081.
- [19] J. Zheng, C. Liu, M. Tian, X. Jia, E. P. Jahrman, G. T. Seidler, S. Zhang, Y. Liu, Y. Zhang, C. Meng, G. Cao, *Nano Energy* **2020**, *70*, 104519.
- [20] Y. Jiang, D. Ba, Y. Li, J. Liu, *Adv. Sci.* **2020**, *7*, 1902795.
- [21] J. Yan, E. H. Ang, Y. Yang, Y. Zhang, M. Ye, W. Du, C. C. Li, *Adv. Funct. Mater.* **2021**, *31*, 2010213.
- [22] Y. Liu, X. Wu, *Nano Energy* **2021**, *86*, 106124.
- [23] X. Xu, F. Xiong, J. Meng, X. Wang, C. Niu, Q. An, L. Mai, *Adv. Funct. Mater.* **2020**, *30*, 1904398.
- [24] B. Sambandam, V. Soundharajan, S. Kim, M. H. Alfaruqi, J. Jo, S. Kim, V. Mathew, Y. K. Sun, J. Kim, *J. Mater. Chem. A* **2018**, *6*, 3850–3856.
- [25] B. He, Z. Zhou, P. Man, Q. Zhang, C. Li, L. Xie, X. Wang, Q. Li, Y. Yao, *J. Mater. Chem. A* **2019**, *7*, 12979–12986.
- [26] X. Zhang, Y. Tang, P. He, Z. Zhang, T. Chen, *Carbon* **2021**, *172*, 207–213.
- [27] H. Li, T. Zhai, P. He, Y. Wang, E. Hosono, H. Zhou, *J. Mater. Chem.* **2011**, *21*, 1780–1787.
- [28] G. A. Sawatzky, D. Post, *Phys. Rev. B* **1979**, *20*, 1546–1555.
- [29] F. Liu, Z. Chen, G. Fang, Z. Wang, Y. Cai, B. Tang, J. Zhou, S. Liang, *Nano-Micro Lett.* **2019**, *11*, 25.
- [30] Z. Li, G. Liu, M. Guo, L. Ding, S. Wang, H. Wang, *Electrochim. Acta* **2015**, *173*, 131–138.
- [31] X. Ren, Y. Zhai, L. Zhu, Y. He, A. Li, C. Guo, L. Xu, *ACS Appl. Mater. Interfaces* **2016**, *8*, 17205–17211.
- [32] D. Chen, X. Rui, Q. Zhang, H. Geng, L. Gan, W. Zhang, C. Li, S. Huang, Y. Yu, *Nano Energy* **2019**, *60*, 171–178.
- [33] Y. Yang, Y. Tang, G. Fang, L. Shan, J. Guo, W. Zhang, C. Wang, L. Wang, J. Zhou, S. Liang, *Energy Environ. Sci.* **2018**, *11*, 3157–3162.
- [34] H. Qin, L. Chen, L. Wang, X. Chen, Z. Yang, *Electrochim. Acta* **2019**, *306*, 307–316.
- [35] L. Chen, Z. Yang, F. Cui, J. Meng, H. Chen, X. Zeng, *Appl. Surf. Sci.* **2020**, *507*, 145137.
- [36] J. Li, K. McColl, X. Lu, S. Sathasivam, H. Dong, L. Kang, Z. Li, S. Zhao, A. G. Kafizas, R. Wang, D. J. L. Brett, P. R. Shearing, F. Corà, G. He, C. J. Carmalt, I. P. Parkin, *Adv. Energy Mater.* **2020**, *10*, 2000058.
- [37] W. Zhang, Y. Xiao, C. Zuo, W. Tang, G. Liu, S. Wang, W. Cai, S. Dong, P. Luo, *ChemSusChem* **2021**, *14*, 971–978.
- [38] D. Kundu, B. D. Adams, V. Duffort, S. H. Vajargah, L. F. Nazar, *Nat. Energy* **2016**, *1*, 16119.
- [39] B. Sambandam, V. Soundharajan, S. Kim, M. H. Alfaruqi, J. Jo, S. Kim, V. Mathew, Y. Sun, J. Kim, *J. Mater. Chem. A* **2018**, *6*, 15530.
- [40] Z. Wu, C. Lu, Y. Wang, L. Zhang, L. Jiang, W. Tian, C. Cai, Q. Gu, Z. Sun, L. Hu, *Small* **2020**, *16*, 2000698.
- [41] M. H. Alfaruqi, V. Mathew, J. Song, S. Kim, S. Islam, D. T. Pham, J. Jo, S. Kim, J. P. Baboo, Z. Xiu, K. S. Lee, Y. K. Sun, J. Kim, *Chem. Mater.* **2017**, *29*, 1684–1694.
- [42] W. Li, C. Han, Q. Gu, S. L. Chou, J. Z. Wang, H. K. Liu, S. X. Dou, *Adv. Energy Mater.* **2020**, *10*, 2001852.
- [43] M. Yan, P. He, Y. Chen, S. Wang, Q. Wei, K. Zhao, X. Xu, Q. An, Y. Shuang, Y. Shao, K. T. Mueller, L. Mai, J. Liu, J. Yang, *Adv. Mater.* **2018**, *30*, 1703725.
- [44] N. Zhang, Y. Dong, M. Jia, X. Bian, Y. Wang, M. Qiu, J. Xu, Y. Liu, L. Jiao, F. Cheng, *ACS Energy Lett.* **2018**, *3*, 1366–1372.
- [45] C. Zhang, Z. Chen, Z. Guo, X. W. Lou, *Energy Environ. Sci.* **2013**, *6*, 974–978.
- [46] X. Dai, F. Wan, L. Zhang, H. Cao, Z. Niu, *Energy Storage Mater.* **2019**, *17*, 143–150.
- [47] N. Zhang, M. Jia, Y. Dong, Y. Wang, J. Xu, Y. Liu, L. Jiao, F. Cheng, *Adv. Funct. Mater.* **2019**, *29*, 1807331.
- [48] T. Jiao, Q. Y. S. Wu, Z. Wang, D. Chen, D. Shen, B. Liu, J. Cheng, H. Li, L. Ma, C. Zhi, W. Zhang, *J. Mater. Chem. A* **2019**, *7*, 16330–16338.
- [49] L. Ma, N. Li, C. Long, B. Dong, D. Fang, Z. Liu, Y. Zhao, X. Li, J. Fan, S. Chen, S. Zhang, C. Zhi, *Adv. Funct. Mater.* **2019**, *46*, 1906142.
- [50] J. Zhou, L. Shan, Z. Wu, X. Guo, G. Fang, S. Liang, *Chem. Commun.* **2018**, *54*, 4457–4460.

Manuscript received: July 20, 2021

Revised manuscript received: August 22, 2021

Version of record online: September 21, 2021